Journal of
Marine Science and Engineering

MDPI

Article

Acoustic Response of a Vibrating Elongated Cylinder in a Hydrodynamic Turbulent Flow

Giacomo Rismondo, Marta Cianferra and Vincenzo Armenio *

Dipartimento di Ingegneria e Architettura, University of Trieste, Piazzale Europa, 1, 34127 Trieste, Italy
* Correspondence: vincenzo.armenio@dia.units.it

Abstract: The present paper contains the results of the numerical analysis of the interaction between a Newtonian incompressible turbulent flow and a linear elastic slender body, together with the influence of the fluid–structure interaction (FSI) on the noise generation and propagation. The purpose is to evaluate the differences in term of acoustic pressure between the case where the solid body is rigid (infinite stiffness) and the case where it is elastic (finite stiffness). A partitioned and implicit algorithm with the arbitrary Lagrangian–Eulerian method (ALE) is used for the interaction between the fluid and solid. For the evaluation of the turbulent fluid motion, we use a large eddy simulation (LES) with the Smagorinsky subgrid scale model. The equation for the solid is solved through the Lagrangian description of the momentum equation and the second Piola–Kirchoff stress tensor. In addition, the acoustic analogy of Lighthill is used to characterize the acoustic source (the slender body) by directly using the fluid dynamic fields. In particular, we use the Ffowcs Williams and Hawkings (FW-H) equation for the evaluation of the acoustic pressure in the fluid medium. As a first numerical experiment, we analyze a square cylinder immersed in a turbulent flow characterized by two different values of stiffness: one infinite (rigid case) and one finite (elastic case). In the latter case, the body stiffness and mean flow velocity are such that they induce the lock-in phenomenon. Finally, we evaluate the differences in terms of acoustic pressure between the two different cases.

Keywords: large eddy simulation (LES); fluid–structure interaction (FSI); Ffowcs Williams and Hawkings (FW-H); noise generation and propagation

check for updates

Citation: Rismondo, G.; Cianferra, M.; Armenio, V. Acoustic Response of a Vibrating Elongated Cylinder in a Hydrodynamic Turbulent Flow. *J. Mar. Sci. Eng.* **2022**, *10*, 1918. https://doi.org/10.3390/jmse10121918

Academic Editors: Mehmet Atlar, Savas Sezen and Rouseff Daniel

Received: 14 October 2022
Accepted: 2 December 2022
Published: 6 December 2022

1. Introduction

The analysis and prediction of the sound generated by a turbulent flow are of fundamental importance in many engineering applications. An important field of application is acoustic pollution and its effects on the environment, which has led to considerable interest and to the development of different analytical and numerical techniques to perform reliable noise predictions [1,2]. Among others, worth of mention is the analysis of the sound generated by wind turbines, because of its own impact on the environment (see for example [3]). Among the possible noise sources, a relevant one is the vibration of slender bodies immersed in a fluid dynamic field. This is the case, for example, of the vocal chords, of the strings of musical instruments and also of a number of engineering systems, such as the steel cables of bridges, hydrofoils, blades of wind turbines or of helicopters. Typically, the mutual interaction between a flow field and a nonrigid structure (fluid–structure interaction, FSI) gives rise to vibrations of the structure which, in turn, produces a *tonal* noise, where with this term, it is intended a narrow-band acoustic signal. FSI has been a field of intense research because of dangerous aeroelasticity or hydroelasticity phenomena often occurring in engineering (for example the lock-in and fluttering phenomena, etc.). The Commonwealth Advisory Aeronautical Council (CAARC) benchmark is widely used for the validation of different FSI numerical methodologies concerning elastic and slender bodies (see, for example, Huang, Shenghong and Rong [4] and Braun, Awruch and Miguel [5]). Most literature in the field of computational aero/hydroacoustics (CAA/CHA), was initially devoted to the analysis of sound propagation in compressible flow conditions (see, for example, Inoue and Hatakeyama [6] and Marsden et al. [7]) mostly considering 2D cases or archetypal geometrical configurations. It is worth to mention that a single-phase fluid dynamic field may belong to the incompressible or to the compressible flow regime depending on the value of the Mach number ($Ma = \frac{U}{c}$, where U is the flow velocity scale and c is the speed of sound in the medium). In the incompressible flow regime ($Ma < 0.3$), the density variation does not affect the transport of mass and momentum and the mechanical energy is decoupled from the thermal one. Mass and momentum conservation equations assume a simplified form and the pressure loses its own meaning of a thermodynamic quantity. In marine hydrodynamics as well as in environmental and civil engineering fluid mechanics, the incompressible flow assumption is the rule, due to the low values of the Mach number. Obviously, in this case, the hydrodynamic pressure is not representative of the acoustic pressure since the latter is always related to the fluid compressibility. In other words, although from a fluid dynamic point of view the incompressible flow hypothesis is an excellent working assumption, if one is interested in the evaluation of the acoustic field, fluid compressibility must be considered even in the limit of $Ma \to 0$. As we discuss later in the paper, the acoustic analogy allows us to use incompressible flow fields to calculate the acoustic pressure. More recently, the generation and propagation of sound in incompressible flow conditions have been the focus of a large number of research projects. In the literature, the so-called acoustic analogy has been developed and is commonly in use, enabling one to decouple the acoustic problem from the fluid dynamic one. The acoustic analogy theory was developed by Lighthill [8], and it consists in recasting the compressible Navier–Stokes equations in the form of an inhomogeneous wave equation. The source term of the latter comes directly from the fluid dynamic fields. This numerical methodology has been used by a number of authors (see [9]) and improved over the years. The research group in hydraulics of the University of Trieste has recently contributed in the field (see [10–12]). Specifically, in [10], the authors investigated the acoustic signature of archetypal geometries, namely a sphere, a cube and a prolate spheroid in a turbulent flow at $Re = 5000$. The authors used a large eddy simulation (LES) for the evaluation of the fluid dynamic incompressible flow and the integral formulation of the wave equation first obtained by Ffowcs Williams and Hawkings (FW-H) [13] for the evaluation of the acoustic field. In [11], the authors proposed a novel computational method for the analysis of the noise contribution coming from the wake of the body (i.e., a slender square cylinder), whereas in [12], the authors analyzed the noise generated by a ship propeller. In all cases examined, the body was considered rigid, although it is well established that, in some cases, the flexibility of a slender body may produce a fluid–structure interaction with consequences on the acoustic response of the structure. The goal of the present study is to take a step forward to evaluate the noise generated by a nonrigid slender body to detect differences between the ideal rigid-body case and the more realistic case of an elastic body. This is, indeed, the case in a number of applications both in the field of hydroacoustics and in aeroacoustics.

Here, we consider a case where a simple body (a square cylinder, such as that of [11]) placed over a rigid wall and made of a linear elastic material is immersed in a flow and interacts elastically with it, hence working in the hydroelastic regime. The study is carried out numerically, using an LES for the evaluation of the hydrodynamic field and the computational hydroacoustics (CHA) for the evaluation of the noise. The direction along which the study is carried out is the identification of the differences between the two cases (rigid versus flexible body) evaluated in terms of the acoustic pressure and characteristics of the turbulent flow. The computational cost required by a numerical analysis of interaction between fluid and structure is high. As a result, an initial analysis and feasibility study is carried out in this study, limiting the required computational cost as much as possible, with the ultimate goal of continuing the research in a more detailed way once the feasibility of the methodology has been assessed.

2. Materials and Methods

The numerical model is composed of three main steps: we use the incompressible Navier–Stokes equations to evaluate the fluid dynamic field (pressure and velocity) together with the momentum conservation law for a linear elastic solid to simulate the vibration of the solid; finally, we use the direct integral formulation of the FW-H equation to calculate the acoustic pressure. The solvers for the fluid motion and for the solid vibration are coupled, through an iterative FSI (fluid–structure interaction) algorithm because of the mutual interaction between the two systems.

2.1. Equations for the Fluid Motion

The governing equations for the motion of a single-phase incompressible and Newtonian fluid are the Navier–Stokes equations. The equations written over a dynamic mesh that deforms in time read as:

$$\nabla \cdot (\mathbf{u} - \mathbf{u}_m) = 0 \tag{1}$$

$$\rho(\frac{\partial \mathbf{u}}{\partial t} + \nabla \cdot (\mathbf{u}(\mathbf{u} - \mathbf{u}_m))) = -\nabla p + \mu \nabla^2 \cdot \mathbf{u} \tag{2}$$

where $\mathbf{u}$ and p are the velocity and hydrodynamic pressure, respectively, ρ and μ are the density and the dynamic viscosity of the fluid and $\mathbf{u}_m$ is the mesh deformation rate, given by $\frac{d\mathbf{v}_m}{dt}$, in which $\mathbf{v}_m$ is the mesh displacement vector obtained by the solution of the Laplace equation:

$$\nabla^2 \cdot \gamma \mathbf{v}_m = 0 \tag{3}$$

which has as boundary conditions $\mathbf{v}_m = \mathbf{v}$, meaning that at the interface, the mesh displacement of the liquid phase and the displacement of the solid wall must be equal.

2.2. Equation for the Solid Motion

The momentum equation for an elastic solid, with the second Piola–Kirchoff stress tensor, is:

$$\rho_s \mathbf{f} + \nabla \cdot (\frac{1}{J} \mathbf{F} \mathbf{S} \mathbf{F}^T) = \frac{D^2 \rho_s \mathbf{v}}{Dt^2} \tag{4}$$

where $\mathbf{v}$ is the displacement, ρ_s is the density, $\mathbf{f}$ represents the volume force, $\mathbf{F}$ is the strain gradient tensor defined as $F = I + \nabla \mathbf{v}$, $\mathbf{S}$ is the second Piola–Kirchoff stress tensor and $J = det(F)$; The second Piola–Kirchoff stress tensor relates forces in the reference configuration to surfaces in the reference configuration. The forces in the reference configuration are obtained via a mapping that preserves the relative relationship between the force direction and the surface orthogonal to it, in the current configuration.

2.3. Fluid–Structure Interaction Equations

The coupling is based on setting proper boundary conditions at the interface between the two systems. Namely, the BCs are:

$$\sigma_f \cdot \mathbf{n}_f = \sigma_s \cdot \mathbf{n}_s \tag{5}$$

$$\mathbf{u} \cdot \mathbf{n}_f = \frac{d(\mathbf{v} \cdot \mathbf{n}_s)}{dt} \tag{6}$$

That is, the pressure and normal component of the velocity at the interface between the fluid and the solid must coincide. The interaction between the solid and the fluid motion is computed using a partitioned algorithm, which makes use of two different solvers for the fluid and the solid part respectively. The algorithm exchanges information, respectively, between one solver and the other. The information, before being taken in a definitive way, enters in an iterative loop until convergence using an implicit method ("2-WAY"). Both solvers are based on the finite volume discretization method and require the use of a deformable mesh. Consequently, at each time step, the mesh is geometrically modified congruently to the deformations of the linear elastic beam. The method adopted is called

ALE because the fluid is solved through an Eulerian approach, taking into account the deformation of the mesh, while the solid is solved through a Lagrangian approach. Finally, the mesh is deformed at the interface and diffused in the interior through a Laplace equation.

2.4. Ffowcs Williams and Hawkings Acoustics Equation

Ffowcs Williams and Hawkings [14] generalized the Lighthill's equation in the presence of a moving solid immersed in a fluid arriving at the following formulation:

$$\begin{aligned}4\pi\hat{p}(\mathbf{x},t) = {} & \frac{\partial}{\partial t}\int_S \frac{\rho v_n}{r[1-M_a]_\tau}dS + \frac{1}{c_0}\frac{\partial}{\partial t}\int_S \frac{p\hat{n}_i\hat{r}_i}{r[1-M_a]_\tau}dS \\ & + \int_S \frac{p\hat{n}_i\hat{r}_i}{r^2[1-M_a]_\tau}dS + \frac{1}{c_0^2}\frac{\partial^2}{\partial t^2}\int_V \frac{T_{rr}}{r[1-M_a]_\tau}dV \\ & + \frac{1}{c_0}\frac{\partial}{\partial t}\int_V \frac{3T_{rr}-T_{ii}}{r^2[1-M_a]_\tau}dV + \int_V \frac{3T_{rr}-T_{ii}}{r^3[1-M_a]_\tau}dV\end{aligned} \tag{7}$$

where $\hat{p}$ is the acoustic pressure, $r = |\mathbf{x}-\mathbf{y}|$ is the distance of the observer from the source, $\hat{r} = (\mathbf{x}-\mathbf{y})/r$, M_a is the Mach number, $T_{rr} = T_{i,j}\hat{r}_i\hat{r}_j$ with $T_{i,j} \sim \rho u_i u_j$ is the Lighthill tensor and T_{ii} its trace.

The first integral term is known as a thickness noise component. It represents the noise generated by the displacement of the fluid mass caused by the movement of the body (in our case the vibration of the cylinder), the second and third terms depend directly on the hydrodynamic pressure acting over the body and are referred to as the loading noise components. The latter three volume integrals are known as quadrupole noise terms and take into account all possible nonlinear sources occurring in the flow field.

2.5. The Numerical Method

The Navier–tokes equations were solved using a large eddy simulation (LES), which provides a three-dimensional time-dependent representation of the actual turbulent field. In an LES, the large, anisotropic and energy-carrying turbulent structures are solved directly through a 3D time-dependent numerical simulation, whereas the small, more isotropic and dissipative structures are parametrized by means of a subgrid scale (SGS) model. Literature studies have proven that the SGSs of motion do not contribute significantly to noise production. Similarly, these dissipative structures are ineffective in the mutual interaction between the fluid and the solid. As the SGS model, we used the standard Smagorinsky model with $C_s^2 = 0.028$ in conjunction with an equilibrium wall-layer model, to skip the direct resolution of the viscous sublayer. A detailed discussion on the wall-layer model is found in [12]. The equations were solved using the PISO algorithm, as implemented in the open-source numerical framework OpenFoam. We used the extended version foam-extend 4.0, which contains the FSI numerical algorithm (the reader is addressed to foam-extend.org for more information). The acoustic postprocessing was carried out using a homemade utility built within the OpenFoam library. The time advancement of the algorithm for the fluid motion was carried out using the implicit second-order (Crank–Nicolson) scheme. For spatial discretization, we used the second-order Gauss integration scheme with a linear interpolation. Further, for the Laplacian term, we used the Gauss integration scheme with a correction of the skewness. In this way, we avoided instability phenomena that might be triggered by excessive deformation of the mesh. We used the GAMG multigrid method to solve the Poisson equation for pressure, using a smoother based on the Gauss–Seidel scheme. We used the PBICG method for the velocity components and the turbulent SGS viscosity. Finally, we used the nonorthogonal corrector, because the mesh deformed in the FSI case. The equation for the deformation of the solid was solved using the *unsTotalLangragianSolid* solver. The time derivative of the displacement was discretized using a first-order explicit Euler method. For spatial discretization, we used the Gauss integration method with a least squares interpolation method (leastSquare). The solution algorithm for the solid movement was the PCG method with a relaxation factor of 0.5. We used the dynamic Aitken relaxation factor to enhance the convergence of the residuals of the coupling equations, reported above. We set the factor at 0.1 and used 20 iterations per time step. The fluid solution algorithm was, overall, second-order accurate, whereas the solution algorithm for the solid was second-order accurate in space and first-order accurate in time. Finally, once the FSI algorithm had been applied, the fluid dynamic data were stored at specific time instants and postprocessed by the acoustic solver. The latter solved the advective form of the FW-H equation described with details in [10,11]. The method would require the evaluation of the integral terms at the time τ different from the time t at which the data are available. This is known as the *time-delay problem*, which makes the evaluation of the volume terms computationally unaffordable. However, [11] introduced the maximum frequency parameter (MFP), which informs on the range of frequencies which are unaffected by the approximation $\tau = t$. Specifically, the condition required for a correct evaluation of the noise associated with a certain frequency is $MFP > 1$. The fulfillment of this condition was verified for the case under investigation.

2.6. Numerical Setup

We considered a simple geometry, namely, a square cylinder mounted over a plane wall in an incompressible turbulent flow (Figure 1). It was substantially different from the case of [10,11], since it belonged to the class of flows classified as *junction flows*. In particular, a horseshoe vortex developed at the junction making the flow field substantially three-dimensional. The frame of reference had the x-axis along the fluid motion, the $y-$axis in the cross stream direction parallel to the wall and the z-axis parallel to the axis of the cylinder. The inlet flow was uniform with velocity $U_0 = 10$ m/s along the x-direction. The square cylinder had a side $d = 0.4$ m and a length $h = 30d$. The value of kinematic viscosity was chosen in such a way as to obtain a value of the Reynolds number of $Re = 4000$, based on the side d. This value was large enough to generate an energetic turbulent wake, characterized by a wide energy spectrum, and, at the same time, computationally manageable.

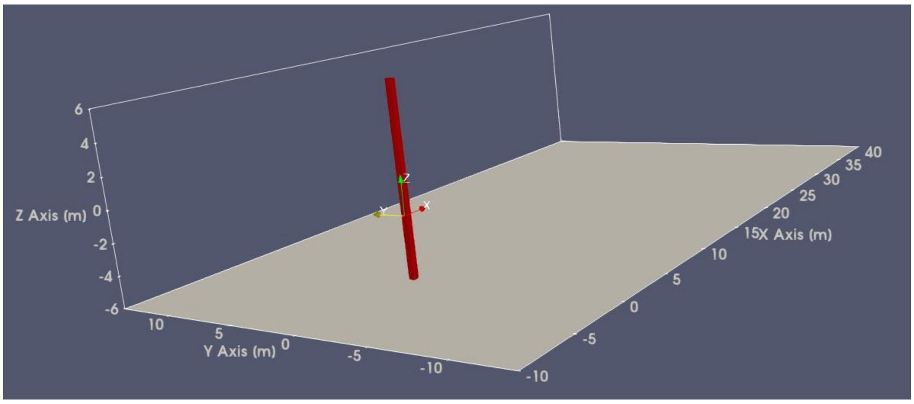

Figure 1. Sketch of the problem under investigation and numerical domain.

The domain was $125d \times 75d \times 50d$ long in the $x-$, $y-$, $z-$direction, respectively, (see Figure 1 for the frame of reference). The center of the cylinder was placed at $25d$ from the inflow plane of the domain.

As boundary conditions, we set the wall-layer model at the surface of the cylinder and at the bottom wall and the symmetry condition at the lateral and top boundaries of the domain; we imposed a velocity ($u = U_0$) and zero gradient for the pressure at the inflow boundary and a zero gradient for the velocity, and we imposed arbitrary pressure $p = 0$ at the outflow boundary.

We adopted quite a coarse mesh (1,193,000 number of cells) to reduce the computational efforts, which was allowed by the use of the wall-layer model approach.

In the x–y plane, the minimum cell length, located near the body, was $\Delta x = \Delta y = 0.09d$ and the maximum cell length in the far field region was $2.9d$. The grid resolution along the z-direction was uniform with $\Delta z = 0.75d$. A zoom of the mesh around the cylinder is shown in Figure 2. We also expressed the cell dimension in wall units $s^+ = \nu/(u_\tau\ s)$ with s a generic direction. The friction velocity was calculated as $u_\tau = \sqrt{\tau_w/\rho}$, with the bulk wall shear stress $\tau_w = C_f\ 0.5\rho U_0^2$ and $C_f = [2log(Re) - 0.65]^{-2.3}$. With these values, the grid resolution used by [10] was $\Delta x^+ \approx 20$, $\Delta y^+ < 1$ at the walls of the cylinder and $\Delta z^+ \approx 20$, because the viscous sublayer was directly resolved there (wall-resolved LES).

Our resolution was $\Delta x^+ = \Delta y^+ \approx 30$ at the walls of the cylinder and $\Delta z^+ = 250$. In our case, we skipped the resolution of the thin viscous sublayer, still maintaining a fine resolution in the wake, to reduce the computational cost while holding the resolution needed for an accurate prediction of the fluid–acoustic field. The present resolution at the solid walls constitutes the standard for a wall-layer-model LES.

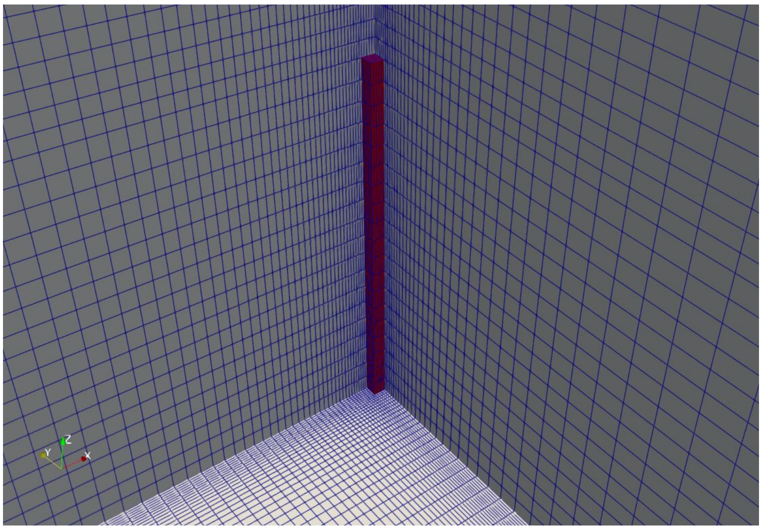

Figure 2. Mesh distribution around the square cylinder.

The density of the fluid was $\rho = 1000\ \mathrm{kg/m^3}$ and the kinematic viscosity $\nu = 1 \times\ 10^{-3}\ \mathrm{m^2/s}$, giving a Reynolds number equal to 4000. The solid was modeled with a density of $\rho_s = 1.85 \times\ 10^5\ \mathrm{kg/m^3}$ and a stiffness module (Young's module) $E = 1 \times 10^{13}\ \mathrm{N/m^2}$. These values were chosen so that the frequency of the first mode of vibration of the cylinder was as close as possible to the frequency of the detachment of the vortices from the cylinder. Consequently, we considered the analytical solution of the homogeneous equation of a cantilever beam for the identification of the frequency of the first fundamental mode. To comply with a Courant number smaller than 0.5, we set the time step equal to 0.001 s. The junction flow introduced substantial variations with respect to the case of a free cylinder, in the region of the three-dimensional horseshoe vortex. To minimize the differences with the case of the free cylinder, for comparison purposes, we considered a region of the cylinder far from the plate, where the flow field was, on average, substantially two-dimensional.

3. Results and Discussion

Here, we first discuss the hydrodynamic field and the modification induced by the resonant vibration of the beam. Successively, we analyze the differences in terms of acoustic signals at different distances from the body.

3.1. The Hydrodynamic Field

For the rigid case, the simulation was run for a nondimensional time $tU_0/D = 700$ and the statistical properties calculated over a time window equal to 375 nondimensional times. The 3D motion of a fluid around a finite size cylinder does not exhibit homogeneous directions, but the length of the cylinder was large enough to consider and compare the data with an equivalent 2D case in the central region of the cylinder (around $z = 0$, namely the midplane of the cylinder). Moreover, the use of such region allowed us to minimize the effect of the presence of the plane wall on the fluid dynamic field. For this reason, velocity components were averaged both in time and space along the z direction for a length ranging from $-5d$ to $5d$. In order to validate the numerical results, we compared the mean velocity profiles with the results obtained in [10,11], where the authors considered a free cylinder and used a wall-resolved LES. In Figure 3, we report the profile of the streamwise velocity component (averaged as discussed above), at various streamwise locations over the lateral side of the cylinder. We observed that the use of the wall-layer model did not reduce appreciably the accuracy of the simulation. A difference was observed in the position of the separation point (about $0.375d$), typical of simulations which make use of wall-layer models. At this location, obviously, we found a maximum difference in the velocity profile of about 8.8%, between the maximum reference velocity and that of our simulation.

The figure also shows the velocity profiles obtained in the case of a flexible cylinder. We note that the velocity profiles were practically not sensitive to the vibration of the cylinder.

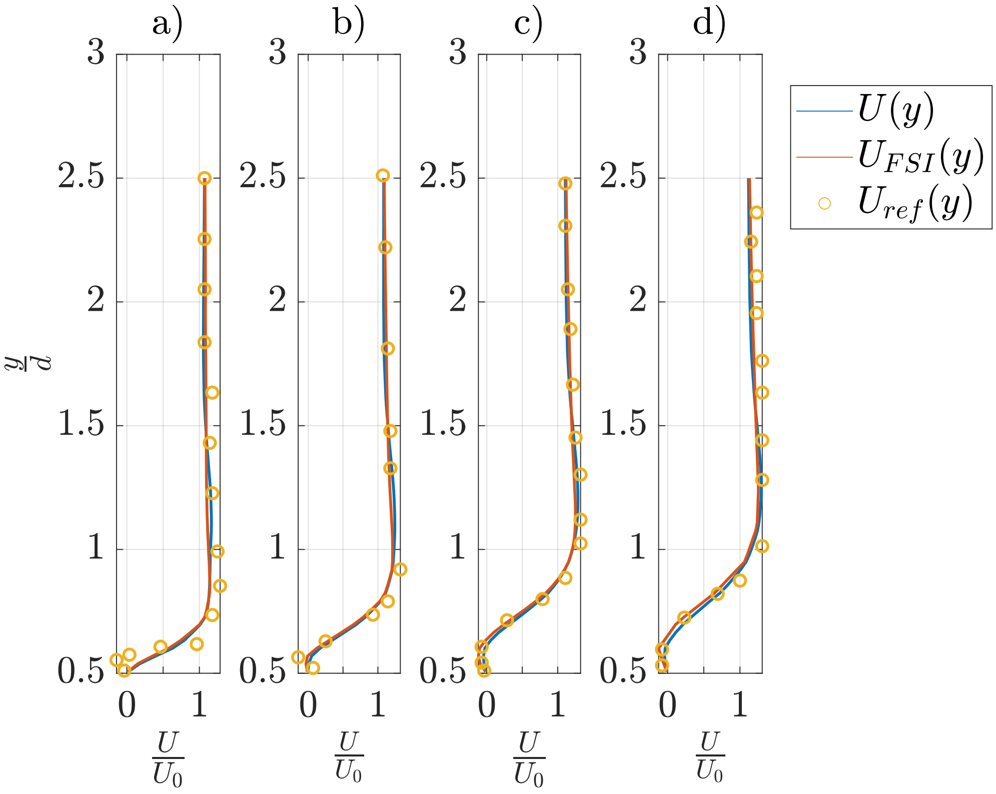

Figure 3. Profiles of the mean streamwise velocity component at different locations: (**a**) $x = -0.375d$, (**b**) $x = -0.125d$, (**c**) $x = 0.25d$ and (**d**) $x = 0.5d$. U_{ref} refers to the results of [10,11].

We also computed the turbulence intensities in the two cases (rigid versus flexible cylinder), identified by the standard deviation of the fluctuating velocity and the Reynolds shear stresses. We observed that the level of fluctuation in the velocity field increased in the case of an elastic body, due to the interaction between the fluid and the structure (Figure 4) and the consequent vibration. The figure shows that the largest differences were for the level of fluctuation along the streamwise direction (about 21.3%) and for the Reynolds shear stress $\langle u'w' \rangle$ (about 21.1%), whereas the differences were less important for the other elements of the Reynolds stress tensor.

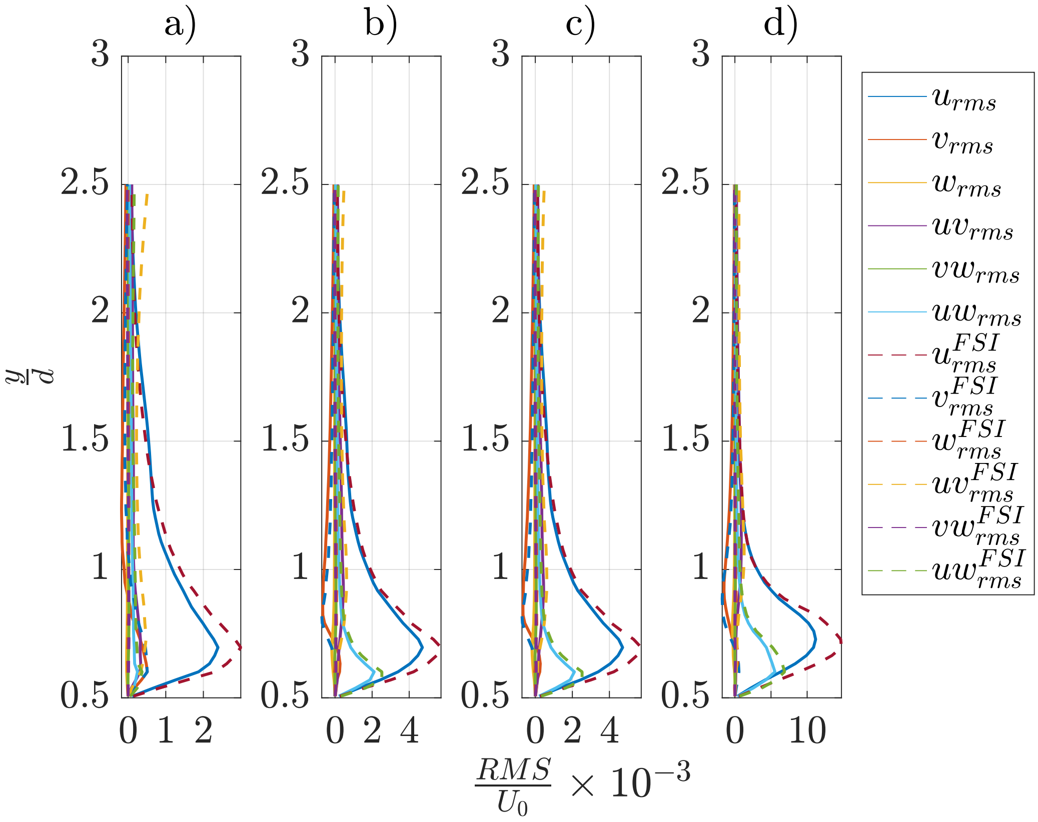

Figure 4. Profiles of turbulence intensities and square root of Reynolds shear stresses for the rigid case and the FSI case, respectively, at streamwise locations: (**a**) $x = -0.375d$, (**b**) $x = -0.125d$, (**c**) $x = 0.25d$ and (**d**) $x = 0.5d$.

We also analyzed the drag and lift coefficients, and, for the rigid cylinder, we compared them with literature values (see Table 1).

Table 1. Drag coefficients and Strouhal number from different simulations.

	Rigid Case	FSI Case	Ref. [10] Fine Grid	Ref. [10] Coarse Grid
$\bar{C}_d$	1.5316	1.440	2.073	1.607
fd/U	0.129	0.132	0.132	/

The lift coefficient was almost zero as expected, since it exhibited periodic oscillations around the zero value. The drag coefficient exhibited a large-scale fluctuation around a mean value together with a number of small-scale fluctuations. Averaging over the time window reported above, we obtained a value close to that obtained with a coarse mesh of the reference study (difference of −4.6% and a bit more underestimated compared to the value obtained with the fine mesh of the reference study (difference of −26.12%). This did not constitute a serious issue for two main reasons. First, the evaluation of the coefficient was very sensitive to the choice of the time window used for averaging the time record; in particular, a very long time window would be necessary to obtain a robust value, which would require an excessively long simulation. Second, since here, we were mainly interested in the analysis of the differences between the rigid and the flexible-body case, a small difference in the value of the drag coefficient was acceptable, in view of the fact that we used a wall-layer model. Finally, we show the time records of the drag and lift coefficients (see Figure 5) and the spectrum of the lift force, which allowed us to evaluate the Strouhal number ($St = fd/U$), the latter being of great importance for the evaluation of the response of the elastic structure. The Strouhal number was underestimated by about

2%, showing the good quality of our simulation. The spectrum exhibited peaks at the main Strouhal frequency as well as at a larger frequency, due to nonlinear characteristics of the wake. In the case of an elastic cylinder, the time records of the drag and lift coefficient appeared somewhat different from the rigid case (see Figure 6). We observed that the vibration of the cylinder reduced the drag and slightly increased the Strouhal number. Moreover, the time record of the lift force appeared modified by the flexibility of the cylinder, with a more energetic low-frequency mode.

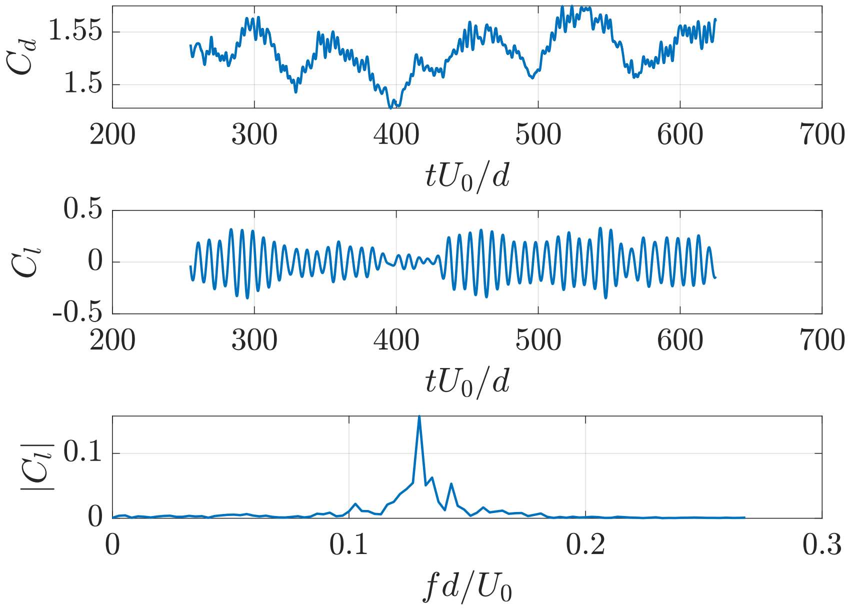

Figure 5. Time record of the drag coefficient (**top** panel); time record of the lift coefficient (**middle** panel); spectrum of the lift coefficient (**bottom** panel). The values refer to the rigid case.

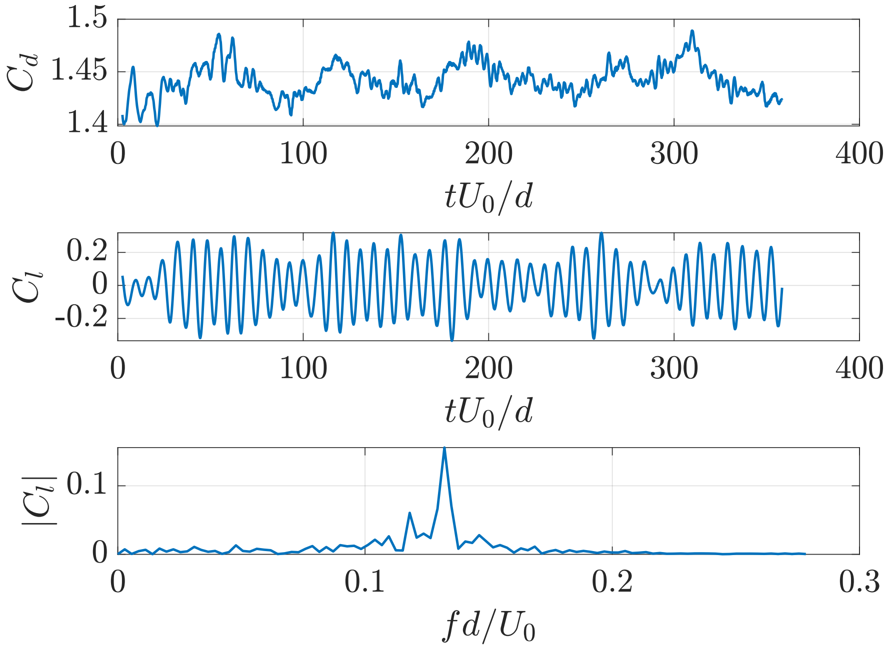

Figure 6. Time record of the drag coefficient (**top** panel); time record of the lift coefficient (**middle** panel); spectrum of the lift coefficient (**bottom** panel). The values refer to the FSI case.

In Figure 7, we report the time record of the displacement of a point positioned at the center of the free edge of the cylinder, in the direction of motion and in the transversal direction, respectively.

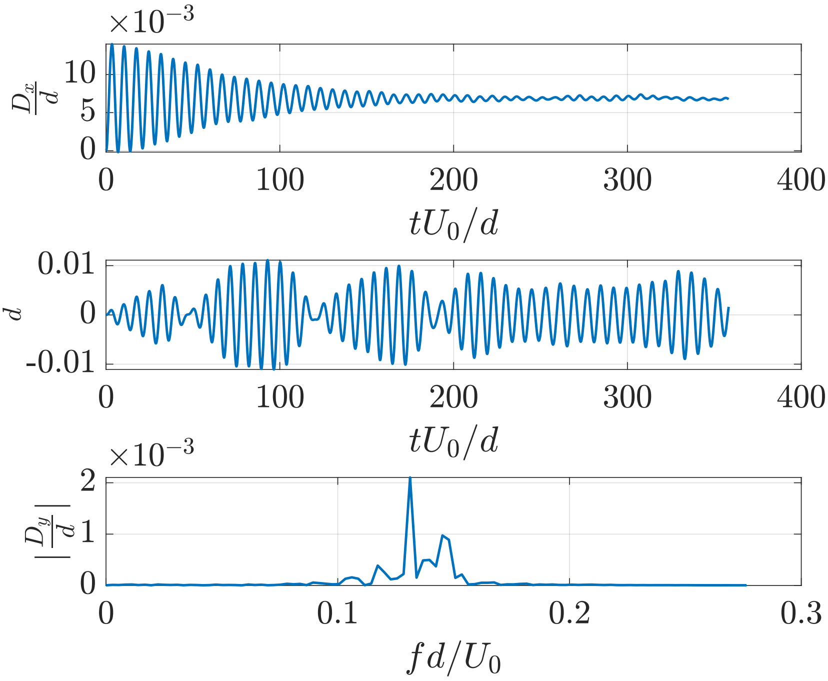

Figure 7. Time record of the displacement of the edge of the cylinder: displacement along the direction of motion (**top** panel); displacement along the transversal direction (**middle** panel), spectrum of the transversal displacement (**bottom** panel).

The displacement in the direction of motion was initially characterized by significant oscillations and successively by a quasi-static condition, characterized by a value of displacement comparable with the theoretical value of a girder embedded and subject to a uniform and stationary load. In fact, if we represented the system as a cantilever beam, characterized by a stiffness $E = 1 \times 10^{13}$ N/m^2 and a length of $l = 12$ m subject to a uniformly distributed load $q = 0.5C_d \rho U_0^2 d = 28,842$ N/m, then the maximum deformation would be equal to

$$v_{max} = \frac{ql^4}{8EI} = 0.0035 \text{ m}.$$

This value was consistent with the mean displacement obtained from the numerical calculation, $v_{max} = 0.0027$ m.

Of particular interest is the vibration in the direction perpendicular to the motion of the fluid. We observed two main behaviors: initially the development was similar to that of a system subject to a dynamic forcing with a frequency slightly different from the fundamental one of the solid, thus leading to beats and the identification of two fundamental frequencies of the displacement signal ($f_1 d/U_0 = 0.130$ and $f_2 d/U_0 = 0.147$), as shown in the bottom panel of Figure 8. After the initial transient, the signal of the lift coefficient and the displacement tended to synchronize over a single fundamental frequency $fd/U_0 = 0.133$ (see Figure 9). A similar behavior was found in [5] where the authors studied the aeroelastic response of the CAARC standard tall building analyzing its structural response under five different wind speed levels.

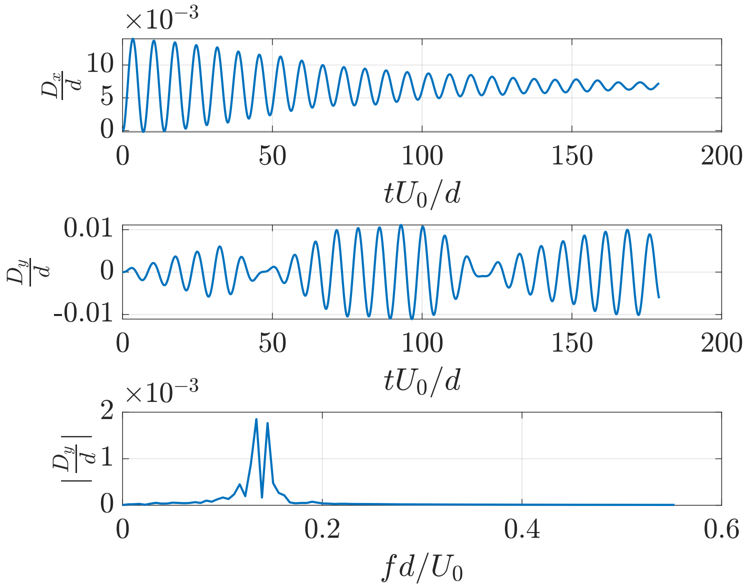

Figure 8. Time record of the displacement of the edge of the cylinder: displacement in the direction of motion (**top** panel); displacement in the transversal direction (**middle** panel); spectrum of the transverse displacement (**bottom** panel); time record in the time interval 0–180 tU_0/d.

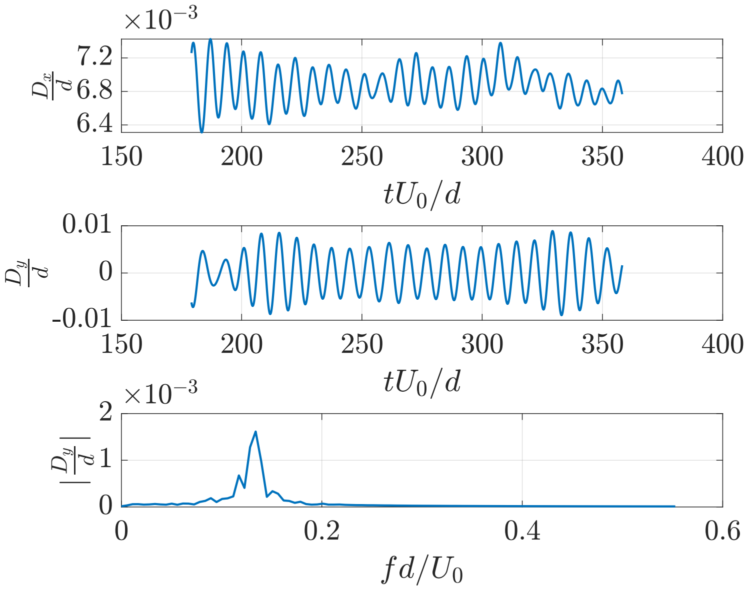

Figure 9. Time record of the displacement of the edge of the cylinder: displacement in the direction of motion (**top** panel); displacement in the transversal direction (**middle** panel); spectrum of the transverse displacement (**bottom** panel); time record in the time interval 180–360 tU_0/d.

Finally, we report the velocity of vibration at the same point discussed above, along the direction of motion and in the transversal direction, respectively (see Figure 10). We observed a rapid decay in the streamwise direction, after the initial transient, whereas an almost steady oscillatory behavior was observed in the transversal direction, associated to the steady vibration of the body. Of note, the vibrational velocity was about three orders of magnitude smaller that the main stream velocity.

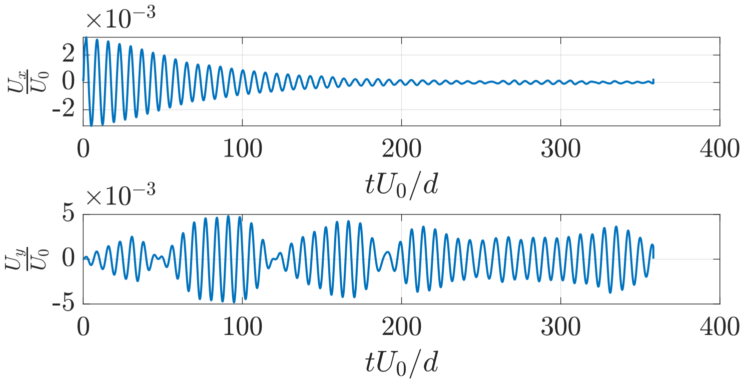

Figure 10. Time record of the velocity of vibration or the edge of the cylinder: velocity component in the direction of motion (**top** panel); velocity component in the transversal direction (**bottom** panel).

3.2. The Acoustic Field

In this section, we report the numerical results of the acoustic pressure obtained from the application of the FW-H equation. Of particular interest is the evaluation of the differences in the acoustic field between the two cases, namely rigid versus elastic case. In order to evaluate the acoustic field, we analyzed the acoustic pressure in terms of root mean square (rms) in polar coordinates. The part of the solid considered for the acoustic analysis was in the range $-6d \leq z \leq +6d$. The volume considered for the FW-H equation was chosen in order to keep the microphones outside the volume of integration. At this stage, we did not calculate the loading term associated to the lower wall (bottom patch), and we did not consider the scattering effect associated to the lower boundary either. We compared the results obtained in the rigid case with those of the elastic one. We calculated the directivity plot of the acoustic pressure at different points placed over concentric circles around the body, placed over a plane orthogonal to the axis of the cylinder at a distance $6d$ from the edge; the radii of the circles were, respectively, $1d$, $5d$, $10d$, $100d$, $200d$, $300d$ and $600d$. For the points very close to the body ($r = 1d$), we evaluated the acoustic pressure with the linear part of the FW-H equation only. Indeed, in that case, it is well known that the linear contribution to the noise is dominant. For the other distances, we considered all terms and compared separately the linear and the nonlinear parts of the FW-H equation.

In Figure 11, we observe that, near the source ($r = 1d$), the vibration of the cylinder induced a noise more intense compared to that of the rigid cylinder case. Specifically, the vibrational velocity of the body produced, from one side, a nonzero value of the thickness term of the FW-H equation and, from the other side, a more intense acoustic pressure. The dipolelike shape of directivity was maintained with larger values of the acoustic pressure associated to the vibration.

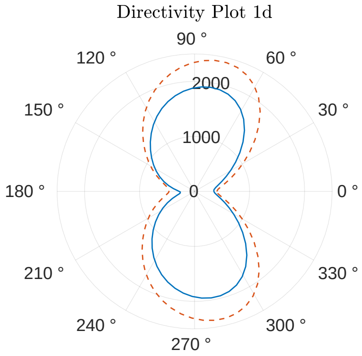

Figure 11. Directivity plot of p_{rms} [Pa] determined by the linear solution of the FW-H equation at $r = 1d$: solid line, rigid cylinder; dashed line, elastic cylinder.

From Figure 12 and beyond, it is possible to figure out that with an increasing distance from the body, the difference between the rigid case and the elastic one became less and less intense, from the point of view of the linear terms of the FW-H equation. However, regarding the nonlinear terms, Figure 13 shows that substantial differences were evident in the presence of a vibration of the structure, which had to be ascribed to the modification of the turbulent field (see Figure 4). The differences between the rigid cylinder case and its flexible counterpart were well visible at all distances examined; in particular, the amplitude as well the shape of the quadrupole changed from one case to the other. Near the body ($r = 5d$), we did not observe appreciable differences from the point of view of the preferred directions of propagation of the acoustic pressure; rather, the intensity was larger in the elastic case. Increasing the distance from the source produced a significant variation of the preferred directions of propagation of the acoustic pressure. This meant that the behavior of the turbulent wake was substantially different in the two cases examined. The total noise, the sum of the linear and of the nonlinear contributions, is plotted in Figure 14. It is interesting to note that in the near-to-intermediate field, the nonlinear part of the noise was dominant and thus the nonlinear terms of the FW-H equation dominated near the cylinder, while with an increasing distance from the source, the linear terms dominated the acoustic pressure.

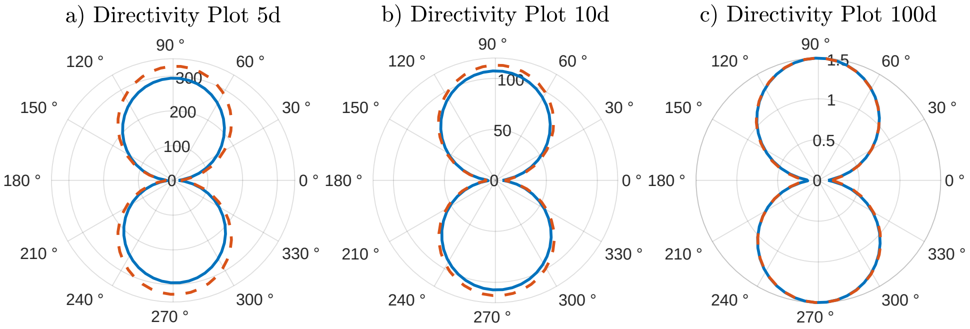

Figure 12. Directivity plot of the p_{rms} [Pa] determined by the linear solution of the FW-H equation on points placed on concentric circles at (**a**) $r = 5d$, (**b**) $r = 10d$ and (**c**) $r = 100d$. Solid line, rigid cylinder; dashed line, flexible cylinder.

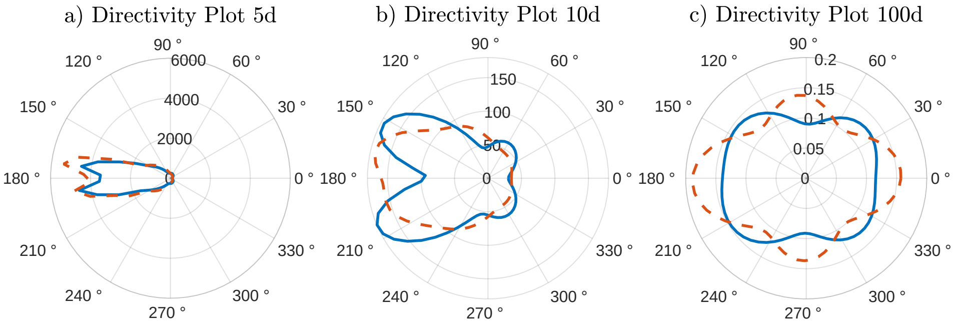

Figure 13. Directivity plot of the p_{rms} [Pa] determined by the nonlinear solution of the FW-H equation on points placed on concentric circles at (**a**) $r = 5d$, (**b**) $r = 10d$ and (**c**) $r = 100d$. Solid line, rigid cylinder; dashed line, flexible cylinder.

Beyond $r = 100d$, we did not observe significant differences between the rigid case and the elastic one, with regards to the linear terms, whereas differences persisted in the nonlinear terms (not shown). With regard to the nonlinear terms, when increasing the distance from the body, the preferred directions of propagation of the sound pressure tended to coincide between rigid and elastic case, until the formation of an almost perfect quadrupole at a distance of $600d$ (see Figure 15). However, as is well known from the classical theory, at that distance from the body, the linear terms dominate and, consequently, differences between the two cases are not appreciable.

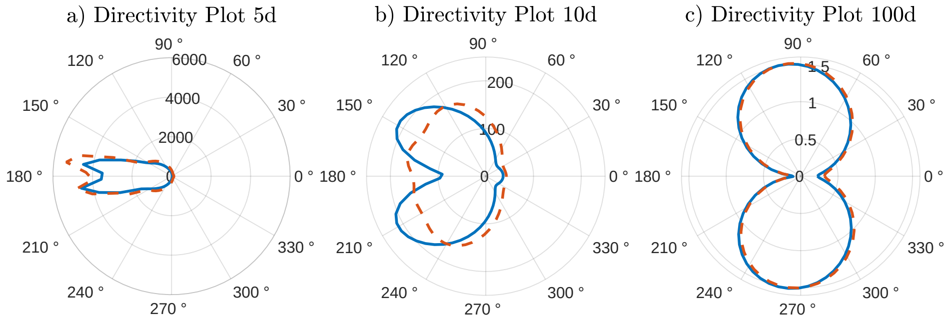

Figure 14. Directivity plot of the p_{rms} [Pa] determined by the solution of the FW-H equation on points placed on concentric circles at (**a**) $r = 5d$, (**b**) $r = 10d$ and (**c**) $r = 100d$. Solid line, rigid cylinder; dashed line, flexible cylinder.

Overall, we noted that in the near-body region, the intensity of the acoustic pressure was larger in the FSI case due to the presence of the thickness term and to an enhanced loading term, whereas in the very far field, the differences between the two cases tended to disappear. The near-to-intermediate field was substantially affected by the elasticity of the body because of the nonlinear contributions. This behavior reflected the fact that the elasticity of the body reduced the formation of large-scale turbulent structures in the wake and increased the number of small-scale turbulent eddies. However, since in the far field, their contribution to the noise was some orders of magnitude smaller than that of the linear term of the FW-H equation, we could say that in the far to very far field, the effect of a small-amplitude resonant vibration was not perceptible in the acoustic field.

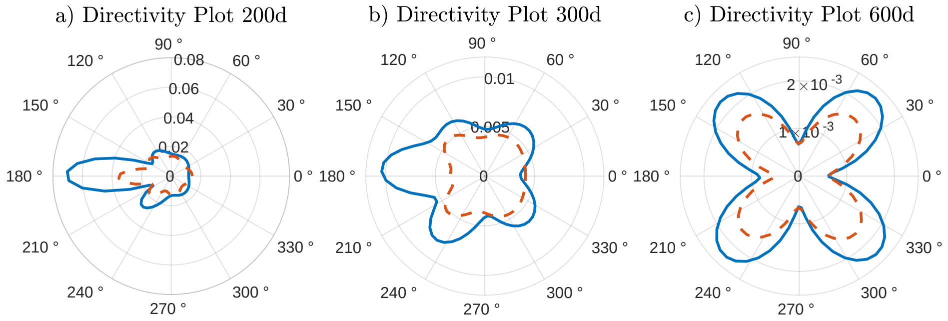

Figure 15. Directivity plot of the p_{rms} [Pa] determined by the nonlinear solution of the FW-H equation on points placed on concentric circles at (**a**) $r = 200d$, (**b**) $r = 300d$ and (**c**) $r = 600d$; the solid line is the rigid case and the dashed line is the FSI case.

Finally, we report the decay of the rms of the total acoustic pressure along the direction of motion and the transversal direction, respectively, in Figure 16. Along the x-direction, a slightly higher intensity was observed in the elastic body case, and the decay of the acoustic energy was piecewise linear (in the log–log plot). In the transversal direction, the difference between the rigid case and the elastic one was significant in the near field only, and the decay was strictly linear in the log–log plot in the intermediate-to-far field. Specifically, the acoustic pressure was substantially larger in the very near field in the elastic case; then, as the distance increased the signals overlapped, consistent with the results of the previous section. The decay of the acoustic pressure in the direction of motion initially was proportional to $\propto r^{-3}$ and as the distance increased the decay became proportional to $\propto r^{-2}$, while in the transverse direction the decay was proportional to $\propto r^{-2}$.

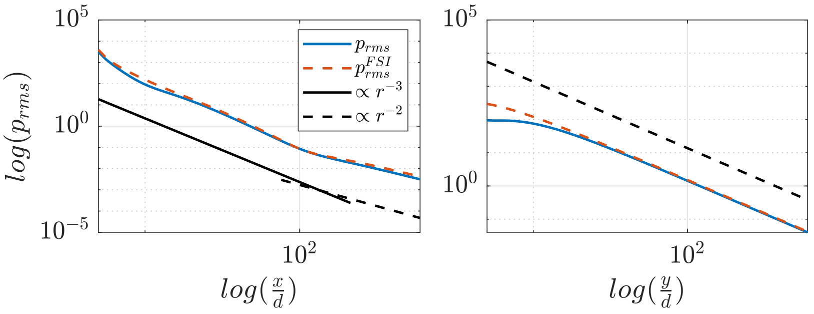

Figure 16. Decay of the acoustic pressure rms along the x-direction (**left**) and the y-direction (**right**): rigid body case, solid blue line; flexible body case, dashed orange line; solid black line, $\propto r^{-3}$; dashed black line, $\propto r^{-2}$.

4. Conclusions

In the present study, we investigated the differences that may occur between the sound generated by a rigid slender body and that given by an equivalent linear elastic body, both immersed in a turbulent flow field. The structural characteristics of the solid were such that the first mode of vibration was excited through the von Karman vortex sheet developing in the wake. In order to correctly detect the interaction between fluid and structure and the implications for the noise generated by the body, we took advantage of the acoustic analogy. First, the hydrodynamic field was obtained through a large eddy simulation of the turbulent field, coupled with the equation for the deformation of a solid body by means of the ALE (arbitrary Lagrangian–Eulerian) algorithm. The numerical solution was successively used by the acoustic solver, which was based on the FW-H equation. We considered a slender square cylinder immersed in a uniform current, characterized by a Reynolds number of 4000. The solid was considered as characterized by two different values of stiffness, one infinite and one finite, in order to evaluate the differences between the rigid and the elastic case. First, we analyzed the hydrodynamic field and we found that, although the mean field was nearly unaffected by the vibration of the solid, the turbulent fluctuations were substantially enhanced by the fluid–structure interaction. The elastic case was characterized by a larger Strouhal number (about 6% higher than the one associated with the rigid case) and a reduced drag coefficient (about 2.27% lower than the rigid case). Subsequently, we evaluated the acoustic response of the structure in terms of directivity plot of the acoustic pressure and compared the noise generated in the two cases discussed above. The analysis showed that due to the substantial variation of the pressure and velocity fluctuating field associated with the vibration of the solid, the interaction between the fluid and the elastic structure significantly modified the acoustic signature of the body. In particular, the very near field was strongly affected by the vibration of the solid, basically because of the vibrational velocity of the body and the associated pressure field. The near-to-intermediate field was controlled by the nonlinear terms and, consequently, by the wake, which was substantially altered by the fluid–structure interaction. The far to very far field remained little affected by the vibration, since the modification of the pressure/velocity field at the body surface was not able to be propagated at large distances.

Author Contributions: Conceptualization, G.R., M.C. and V.A.; methodology, G.R. and M.C.; software, G.R. and M.C.; validation, G.R. and M.C.; formal analysis, G.R. and M.C.; investigation, G.R.; resources, V.A.; data curation, G.R.; writing—original draft preparation, G.R.; writing—review and editing, M.C. and V.A.; visualization, G.R.; supervision, M.C. and V.A.; project administration, V.A.; funding acquisition, V.A. All authors have read and agreed to the published version of the manuscript.

Funding: This research received no external funding.

Institutional Review Board Statement: Not applicable.

Informed Consent Statement: Not applicable.

Data Availability Statement: Numerical data available upon request.

Conflicts of Interest: The authors declare no conflict of interest.

Abbreviations

The following abbreviations are used in this manuscript:

FSI	Fluid–structure interaction
ALE	Arbitrary Lagrangian–Eulerian
LES	Large eddy simulation
FW-H	Ffowcs Williams and Hawkings
CCARC	Commonwealth Advisory Aeronautical Council
CAA	computational aeroacoustics
CHA	computational hydroacoustics

References

1. Murphy, E.; King, E.A. *Environmental Noise Pollution: Noise Mapping, Public Health, and Policy*; Newnes: London, UK, 2014.
2. Carlton, J.; Vlasic, D. Ship vibration and noise: Some topical aspects. In Proceedings of the 1st International Ship Noise and Vibration Conference, London, UK, 20–21 June 2005 ; pp. 1–11.
3. Saidur, R.; Rahim, N.A.; Islam, M.R.; Solangi, K.H. Environmental impact of wind energy. *Renew. Sustain. Energy Rev.* **2011**, *15*, 2423–2430. [CrossRef]
4. Huang, S.; Li, R.; Li, Q. Numerical simulation on fluid-structure interaction of wind around super-tall building at high reynolds number conditions. *Struct. Eng. Mech.* **2013**, *46*, 197–212. [CrossRef]
5. Braun, A.L.; Awruch, A.M. Aerodynamic and aeroelastic analyses on the CAARC standard tall building model using numerical simulation. *Comput. Struct.* **2009**, *87*, 564–581. [CrossRef]
6. Inoue, O.; Hatakeyama, N. Sound generation by a two-dimensional circular cylinder in a uniform flow. *J. Fluid Mech.* **2002**, *471*, 285–314. [CrossRef]
7. Marsden, O.; Bogey, C.; Bailly, C. Direct Noise Computation of the Turbulent Flow Around a Zero-Incidence Airfoil. *AIAA J.* **2008**, *46*, 874–883. [CrossRef]
8. Lighthill, M.J. On sound generated aerodynamically I. General theory. *Proc. R. Soc. Lond. Ser. Math. Phys. Sci.* **1952**, *211*, 564–587.
9. Wang, M.; Freund, J.B.; Lele, S.K. Computational prediction of flow-generated sound. *Annu. Rev. Fluid Mech.* **2006**, *38*, 483–512. [CrossRef]
10. Cianferra, M. Acoustic Analogies and Large-Eddy Simulations of Incompressible and Cavitating Flows around Bluff Bodies. 2018. Available online: https://hdl.handle.net/11368/2922550 (accessed on 13 October 2022).
11. Cianferra, M.; Armenio, V.; Petronio, A. Numerical prediction of the far field noise generated by a ship propeller. In I*NTER-NOISE and NOISE-CON Congress and Conference Proceedings*; Institute of Noise Control Engineering: North Billerica, MA, USA , 2019; Volume 259, pp. 4146–4157.
12. Cianferra, M.; Petronio, A.; Armenio, V. Non-linear noise from a ship propeller in open sea condition. *Ocean. Eng.* **2019**, *191*, 106474. [CrossRef]
13. Lockard, D.P. An efficient, two-dimensional implementation of the Ffowcs Williams and Hawkings equation. *J. Sound Vib.* **2000**, *229*, 897–911. [CrossRef]
14. Williams, J.F.; Hawkings, D.L. Sound generation by turbulence and surfaces in arbitrary motion. *Philos. Trans. R. Soc. Lond. Ser. A Math. Phys. Sci.* **1969**, *264*, 321–342.